Low-cost flexible plasmonic nanobump metasurfaces for label-free sensing of serum tumor marker

Jinfeng Zhu [a,*], Zhengying Wang [a], Shaowei Lin [b], Shan Jiang [a], Xueying Liu [a], Shengshi Guo [c]

[a] *Institute of Electromagnetics and Acoustics, Xiamen University, Xiamen, 361005, China*
[b] *The First Affiliated Hospital of Xiamen University, Xiamen, 361003, China*
[c] *College of Physical Science and Technology, Xiamen University, Xiamen, 361005, China*

ABSTRACT

The use of plasmonic metasurface for sensing has great potential on label-free detection of human tumor markers, which could benefit clinical examination. In this work, we adopt nanoimprint and plasma etching to optimize the nanofabrication for low-cost flexible plasmonic metasurface sensors with gold nanobump arrays, which enable facile surface bio-functionality, high sensitivity and simple optical measurement in the visible range. A high bulk refractive index sensitivity of 454.4 nm/RIU is achieved for the prototype plasmonic metasurface sensors at the wavelengths from 620 nm to 720 nm. The rapid quantitative tumor marker sensing of carcinoembryonic antigen in human serum samples from less than 10 ng/mL to more than 87 ng/mL is achieved, which demonstrates good agreement with the conventional chemiluminescence immunoassay system and sufficiently covers the threshold tumor marker concentration of 20 ng/mL for early cancer prediction. Our method is capable of low-cost high-throughput manufacturing for flexible lightweight plasmonic metasurface sensors, which will facilitate wide applications on portable biomedical sensing devices for future point-of-care diagnosis and mobile healthcare.

1. Introduction

Plasmonic metasurfaces are the 2-dimensional versions of metamaterials, which commonly consist of an array of unit metal nanostructure elements with specifically designed geometry, size, and orientation (Cai et al., 2015; Chen et al., 2019; Costantini et al., 2015; López-Muñoz et al., 2017; Qin et al., 2016; Reshef et al., 2019; Wang and Zhan, 2016). In the past few years, the research of plasmonic metasurface has attracted significant attention due to the increasing application demand on optical lens, sensing, light trapping, integrated circuit, high-resolution imaging, chemical analysis and photo-thermal manipulation (Bouchal et al., 2019; Hwang and Davis, 2016; Liang et al., 2017; Ndukaife et al., 2014; Tang et al., 2016; Xu et al., 2011; Zhu et al., 2011). Among these investigations, label-free biomolecular sensing based on plasmonic metasurfaces has demonstrated considerable achievements, which benefits from the nanoscale near-field enhancement with high sensitivity and non-destructive operation for high-throughput real-time detection (Cetin et al., 2015; Liu et al., 2018; Zhou et al., 2019). Driven by the intensive demands on fast, highly sensitive and cost-effective biosensing for point-of-care diagnosis and mobile healthcare (Zhang

et al., 2015, 2018), many efforts have been made to improve the performance of plasmonic sensors by using various nanostructured metasurfaces (Cai et al., 2019; Danilova et al., 2018; Tokel et al., 2014; Wang and Fan, 2016).

Plasmonic metasurface biosensors typically need uniform periodic nanostructures with few defects, fine features, and large-area patterns via a low-cost and reproducible fabrication process. However, in order to maintain their high sensing performance, sophisticated nanofabrication methods are usually adopted, such as focused ion beam and electron beam lithography. Based on the serial operation, they usually involve a time-consuming and expensive patterning process on rigid substrates such as silicon, glass or fused silica (Feng et al., 2019; Jackman et al., 2017; Singh, 2016; Špačková et al., 2016). Conventional nanoimprint lithography might be an alternative way to reduce the fabrication cost, but the plasmonic nanostructures have been typically fabricated on costly rigid substrates (Jo et al., 2016). Up to date, the previous efforts still hinder the practical applications of plasmonic metasurfaces, particularly in lightweight, wearable and disposable biosensors. In addition, the bio-compatibility and bio-functionalization of plasmonic metasurfaces are also very critical in practical sensing

---

* Corresponding author.
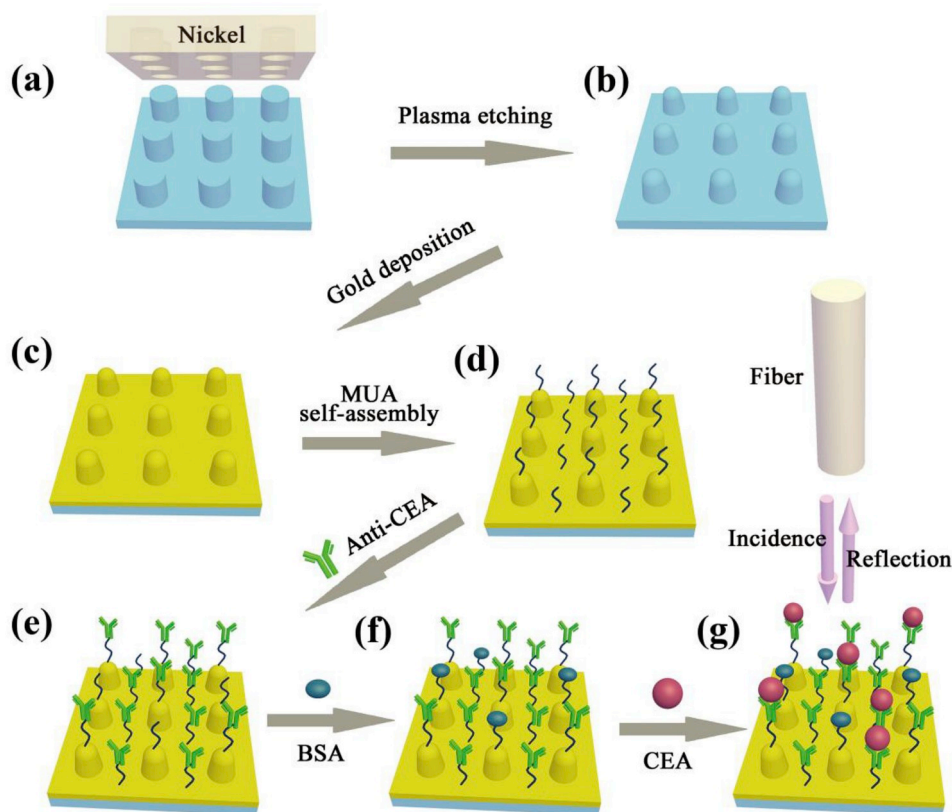 *E-mail address:* nanoantenna@hotmail.com (J. Zhu).

Fig. 1. (a)~(c) Fabrication process of the plasmonic metasurface. (d)~(g) Schematic drawing of bio-functionalization and tumor marker detection.

applications. So far the potential use of low-cost, flexible, disposable plasmonic metasurfaces with biomedical functionalization for high-performance biosensors has yet to be realized.

In this work, we investigate the low-cost flexible bio-functionalized plasmonic metasurfaces for high sensitive label-free detection of tumor marker in human serum samples. The plasmonic metasurfaces with periodic gold nanobumps are fabricated on a flexible lightweight polycarbonate substrate in a resist-free way, which is simply processed by nanoimprint, etching and metal evaporation in a very short time (see Table S1 in the Supplementary Material). Our approach reduces the material cost from \$ 6 to \$ 0.85 and the weight from 1.87 g to 0.42 g for a 2 inch wafer. The low-cost plasmonic metasurfaces optimized by oxygen plasma etching on lightweight plastic substrates demonstrate the enhanced bulk sensitivity and quality factor. Furthermore, the nanobump metasurfaces show high capability for carcinoembryonic antigen (CEA) detection, which makes it potentially suitable for emerging flexible plasmonic biosensing devices.

2. Materials and methods

2.1. Materials and characterization

The polycarbonate slices used as the substrates are purchased from Obducat AB (Lund, Sweden). The self-assembly reagent 11-Mercaptoundecanoic acid (MUA) is from Cool Chemistry (Beijing, China). Phosphate buffer saline (PBS), 1-Ethyl-3-[3-dimethylaminopropyl] carbodiimide hydrochloride (EDC) and N-hydroxysuccinimide (NHS) are purchased from LvYin Reagent (Xiamen, China). Bovine serum albumin (BSA) is from Sangon Biotech (Shanghai, China). CEA and its antibody anti-CEA are from Siemens Healthcare Diagnostics (New York, USA). We use the atomic force microscope (AFM, SPA400) and scanning electron microscope (SEM, Carl Zeiss SIGMA HD) to characterize the morphology of the plasmonic metasurfaces. The energy dispersive spectroscopy (EDS)

combined with the SEM is used to obtain the high-speed elemental mapping on the plasmonic metasurfaces.

2.2. Fabrication of plasmonic metasurfaces

The fabrication work flow is shown from Fig. 1(a) to Fig. 1(c). The periodic nanocylinder arrays are imprinted on the polycarbonate substrate using a 2-inch nickel mold with void nanocylinder arrays by thermal processing at a temperature range between 110 °C and 150 °C under a pressure of 40 bar. After that, the nanocylinders are changed to nanobumps by oxygen plasma under various etching time, and evaporated by 5 nm chromium and 150 nm gold.

2.3. Bio-functionalization of plasmonic metasurfaces

In this process, the plasmonic metasurfaces are bio-functionalized by thiolate modification and covalent immobilization of anti-CEA, as shown from Fig. 1(d)–1(f). At the beginning, they are kept in the 1 mM MUA solution of ethanol for over 12 h, in which a self-assembled MUA monolayer is formed on their top surface. Then, they are cleaned by deionized water thoroughly and kept in a solution with 400 mM EDC and 100 mM NHS for half an hour in order to activate the MUA monolayer (Lee et al., 2015). After that, they are cleaned with deionized water again and incubated by 300 μL anti-CEA PBS solution (40 μg/mL) in a micro-chamber and maintained for 1 h, followed by BSA injection for blocking nonspecific adsorption (Niu et al., 2014). At last, the bio-functionalized metasurfaces are washed by deionized water and ready for use.

2.4. Optical measurement and simulation

A spectrometer with an integrated optical fiber probe (Avantes BV, Apeldoom, Netherlands) is used to measure the reflectance spectra of all
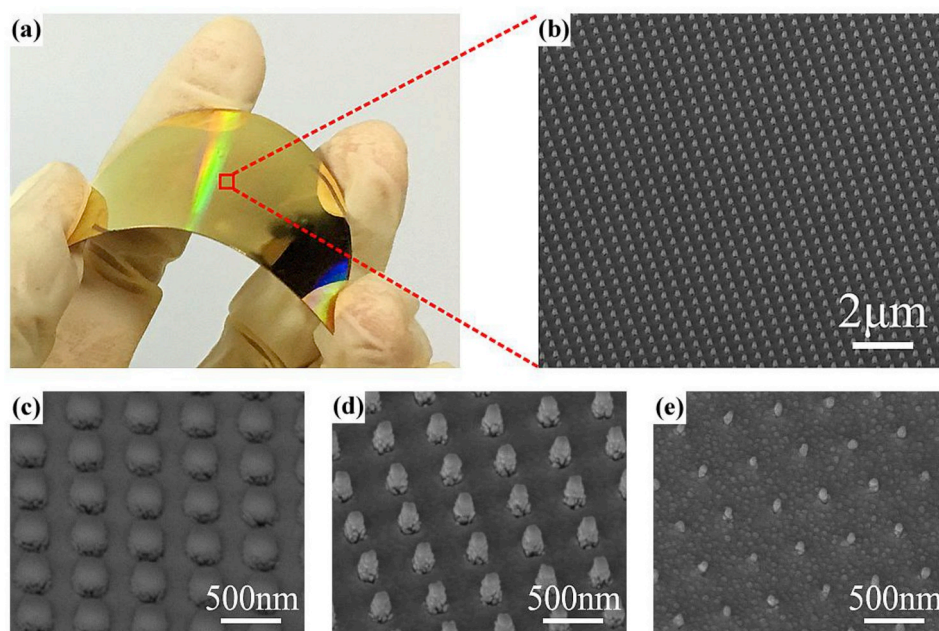
Fig. 2. (a) Photograph of the large-area flexible metasurface and (b) its corresponding SEM image. (c)~(e) SEM images for samples without etching, with 425s etching and with 575s etching, respectively.

plasmonic metasurface samples. The probe has 6 lighting fibers and 1 reading fiber (200 μm core) with the measuring range from visible to near-infrared. In the measurements, the probe is perpendicularly on top of the samples with a distance of about 4 mm and the reflectance from a gold mirror is used as a spectral reference. For the biomolecule detection, the incubation micro-chambers are filled with deionized water.

Optical simulation based on the finite element method is exploited to investigate the optical reflectance from the metasurface by normal incidence and the corresponding plasmonic effects. Infinite unit cells are adopted with Floquet periodic boundary conditions. The dispersive optical permittivity of gold is obtained from the literature (Johnson and Christy, 1972). Adaptive inhomogeneous tetrahedral meshing is used to discretize the simulation model (Zhu et al., 2016). The minimum edge length of the mesh element is set to 0.5 nm to ensure the simulation convergence and reproducibility.

2.5. Specific binding and biosensing of CEA

The detection of CEA is based on its specific binding on the anti-CEA, as shown in Fig. 1(g). In order to indicate the specificity of CEA for biomolecule binding, three kinds of phosphate buffer saline (PBS) solutions of 30 ng/mL CEA, 63 ng/mL AFP, and 30 ng/mL CEA in combination with 63 ng/mL AFP are detected by the bio-functionalized metasurfaces, respectively. Furthermore, the biosensing curve of CEA is confirmed by applying five CEA concentrations from 10 ng/mL to 50 ng/mL. Each metasurface sample is kept inside one incubation micro-chamber with the 300 μL solution for 30 min and measured in the deionized water by the reflectance probe, as shown in Fig. 1(g). In the spectral measurements, three groups of solution are used for each concentration, which are further adopted for *s.d.* calculations.

2.6. Diagnosis of CEA in human serums

All the serum samples are collected from the First Affiliated Hospital of Xiamen University (Xiamen, China) with the consent from the individuals. These samples are tested in advance by the chemiluminescence immunoassay system (ADVIA Centaur XP, Siemens Healthineers). They are stored in the refrigerator at −20 °C and used for the test by the metasurfaces at room temperature after thawing. For each

test, a serum sample of 300 μL is injected and incubated in a microchamber for 30 min. After that, the serum is extracted and the chamber is filled with deionized water. The optical reflectance is measured and compared with that from the original bio-functionalized metasurface for the concentration calculation.

3. Result and discussion

3.1. Plasmonic effects and nanostructure optimization

A simple process based on thermal nanoimprint, plasma etching and gold deposition are adopted to fabricate the flexible wafer-scale plasmonic metasurfaces (Zhu et al., 2017), as shown in Fig. 2 (a) and (b). The nanofabrication is versatile and inexpensive for mass production. The metasurfaces have large areas of uniform periodic gold nanobumps, which facilitate the standardized manufacture for biosensing applications. These metasurfaces act as two-dimensional gratings with rectangular reciprocal lattice vectors, which allows for the excitation of plasmonic resonance by coupling the incident light. The plasmonic resonance wavelengths under normal incidence could be estimated by the following equation (Ghaemi et al., 1998),

$$\lambda_R = P(\epsilon_{Au}\epsilon)^{1/2}[(\epsilon_{Au}+\epsilon)(m^2+n^2)]^{-1/2} \qquad (1)$$

where P, integers (m, n), ϵ_{Au} and ϵ represent the periodicity of gold nanobumps, the grating orders of the corresponding reciprocal vectors, the permittivity of gold and the environmental permittivity at the resonance wavelength, respectively. Equation (1) only considers an ideal lattice of nanostructure with the fixed periodicity P for the estimation of plasmonic resonance wavelength, but it neglects the morphology and size effects of the gold nanostructure (Molen et al., 2004; Gordon et al., 2004). Some previous studies have implied that the morphology and size of the unit element should be well engineered, because they will influence the sensing performance significantly.

In this study, the oxygen plasma etching on the nanostructured polycarbonate is an efficient method to optimize the plasmonic metasurface for high performance optical sensing. As shown from Fig. 2(c)–2(e), we can obtain various gold nanostructures by tuning the oxygen flow rate, radio-frequency power and etching time (Zhu et al., 2012).
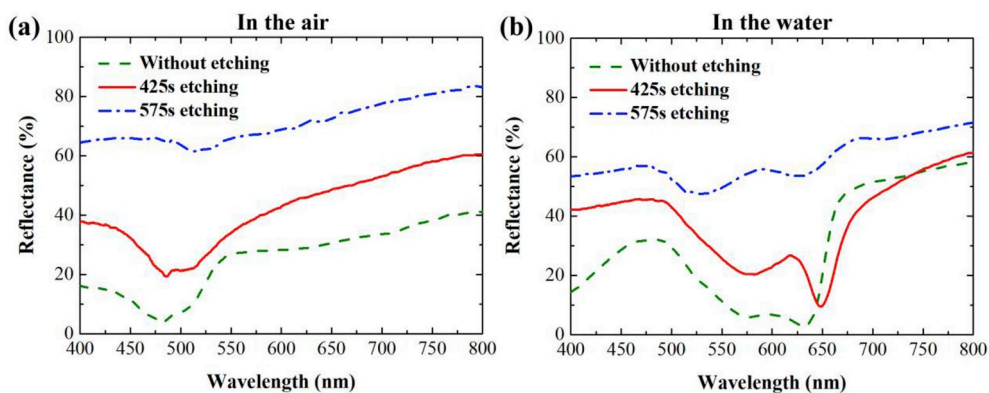
Fig. 3. Reflectance spectra for three kinds of plasmonic metasurfaces fabricated by no etching (0 s), optimal etching (425 s) and over etching (575 s) on polycarbonate nanostructures, respectively. (a) Measurement in the air. (b) Measurement in the water.
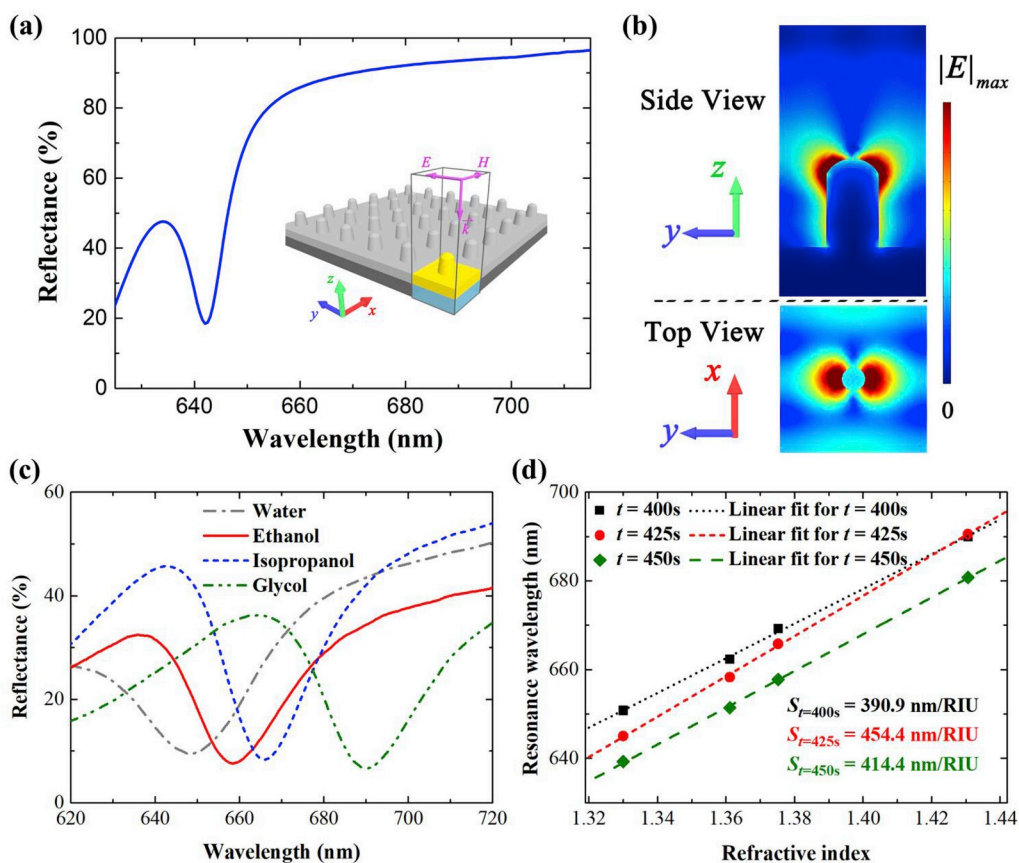

Fig. 4. (a) Simulated reflectance of the plasmonic metasurface in the water, where the inset denotes the simulation model with the unit cell. (b) Electric field distributions at the resonance wavelength. (c) Reflectance spectra for using various solvents. (d) Resonance wavelength as a function of refractive index and etching time with different sensitivities.

The original gold nanocylinders in Fig. 2(c) can be etched into the gold nanobumps in Fig. 2(d), which demands appropriate optimization on nanofabrication. The over etching obtains gold nanodots as shown in Fig. 2(e), but it also brings about an increased roughness of the substrate background. In principle, a high quality factor and a small full wave at half maximum (FWHM) for plasmonic resonance are quite in demand for high performance refractive index sensing. The plasmonic resonance features significantly depend on the size and morphology of the metasurface, and this can be well engineered and optimized by oxygen plasma etching on the polycarbonate nanostructure. As shown in Fig. 3, the nanostructure fabricated without etching demonstrates a large

FWHM and a low quality factor, despite it is in the air or in the water. The sample fabricated by over etching (e.g. 575s) indicates the reflection property in the air like a flat gold film, and shows two obvious resonance dips in the water, but the resonances have low quality factors and large FWHMs. For an optimized etching time of 425s, the metasurface shows the similar plasmonic resonance feature as the over etched one in the air, but it demonstrates a remarkable plasmonic resonance with a narrow FWHM around the wavelength of 650 nm, which is very beneficial for the refractive index sensing. The pronounced differences for the 425s etching between Fig. 3(a) and Fig. 3(b) can be explained as below. In the air, the low order plasmonic resonance is depressed and merged with the
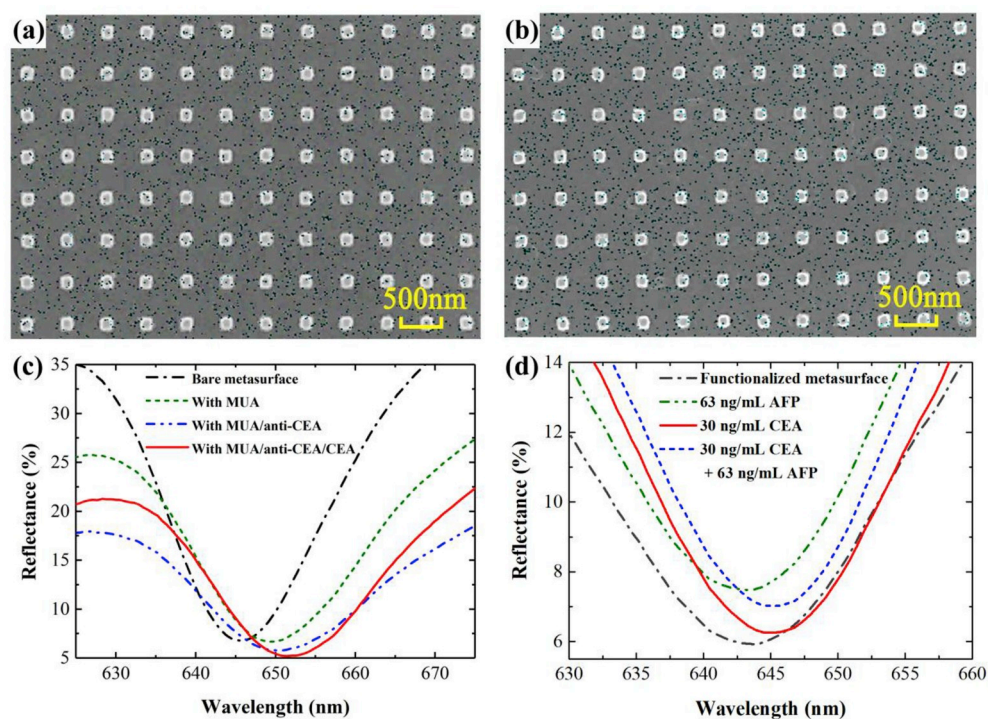
Fig. 5. Nitrogen elemental mapping by EDS (top view, collected by 3 min) for (a) the functionalized metasurface and (b) the metasurface immobilized by CEA, where the blue dots denote the density of nitrogen element. (c) Reflectance spectra for the bare metasurface, metasurface with MUA, metasurface with MUA/anti-CEA, and metasurface with MUA/anti-CEA/CEA, where $t = 425s$. (d) Reflectance spectra for biomolecule specificity test, where $t = 475s$. (For interpretation of the references to colour in this figure legend, the reader is referred to the Web version of this article.)

high order one due to the intrinsic loss in gold below the wavelength of 550 nm, whereas the low order plasmonic resonance in the water can be effectively isolated and shows promising resonance feature as a result of the morphology and size optimization.

3.2. Optical simulation and bulk refractive index sensing

We next reveal the physical insight for plasmonic enhancement effects on the optical sensing by simulation. As shown in Fig. 4(a), the simulated reflectance spectrum for the plasmonic metasurface in the water shows a distinct dip due to the plasmonic resonance in the visible range, whose property is consistent with the measured result. The slight simulation deviation from the measurement might be due to the use of an ideal geometry modeling. As observed in Fig. 4(b), the electric field at the resonance wavelength is significantly enhanced and localized surrounding the top surface and the side of the gold nanobump. Therefore, the near-field enhancement in combination with the good uniformity of the nanostructure will dramatically increase the sensitivity, which statistically reflects the change of local environmental refractive index due to the biomolecular binding on the entire metasurface.

Before the biomolecule detection, the bulk refractive index sensing performance is evaluated experimentally by immersing the plasmonic metasurface in deionized water, ethanol, isopropanol and glycol, respectively (Zheng et al., 2019). As observed in Fig. 4(c), the spectral dip of plasmonic resonance shifts to longer wavelengths due to the increase of refractive index of the environmental liquid, which is consistent with the estimation of Equation (1). The resonance wavelength as a function of environmental refractive index by varying the etching time is shown in Fig. 4(d). The measurement error bars are too small to be observed in the figure. Compared with other etching-time configurations in the experiments, we find that the optimized 425s etching shows the highest sensitivity of 454.4 nm/RIU ($S = \Delta n / \Delta \lambda$), which is competitive with many other plasmonic sensors using conventional complanate arrays (see Table S2 in the Supplementary Material). Thus, the larger bulk refractive index sensitivity implies higher sensing performance for the next biomolecule detection.

3.3. Bio-functionalization and biomolecule specific sensing

With the aim of biomolecule detection, we use the scheme of immunoassay through the reflection type of visible light measurement. The self-assembled monolayer of MUA is applied on the metasurface as an intermediate material layer to immobilize anti-CEA by the way of covalent-bonding for the bio-functionalization of metasurface (Camilo et al., 2019; Liu et al., 2016). The immobilized anti-CEA will selectively capture the CEA from the tested sample for the sensing. By the EDS analysis comparison between Fig. 5(a) and Fig. 5(b), we find that the nitrogen elemental density (a representative element to indirectly denote the increase of the protein content) is obviously increased after the CEA is captured by the anti-CEA-functionalized metasurface. As observed in Fig. 5(c), compared to the spectrum of bare metasurface, the spectra for the metasurface with MUA and the metasurface with MUA/anti-CEA have the redshifts of 3.60 nm and 4.98 nm, respectively, which result from the increase of effective local refractive index induced by the change of surface biomolecule. When we use the metasurface bio-functionalized by anti-CEA for the detection of 10 ng/mL CEA, the plasmonic resonance dip has another red shift of 0.82 nm. The ultimate red shift is correlated with the concentration of CEA, which can be further investigated for CEA detection.

The metasurface immobilized by anti-CEA is developed for the final CEA test of the human serum samples. Nevertheless, the human serum is a complicated mixture with diverse antibodies and antigens, which might interfere the detection result. In order to exclude the possible influences from external interference, we test three kinds of solutions as shown in Fig. 5(d). This figure indicates that there is no change of the resonance wavelength for the 63 ng/mL AFP solution, compared with that of the bio-functionalized metasurface. However, there is the same red shift of about 1.68 nm for both the 30 ng/mL CEA solution and the solution with 30 ng/mL CEA and 63 ng/mL AFP. Due to the biomolecule specificity, the metasurface functionalized by anti-CEA only selectively binds CEA from the solutions, and there is no specific binding of AFP biomolecules on the surface. These results well indicate the immunologic specificity of the bio-functionalized metasurface for CEA detection.
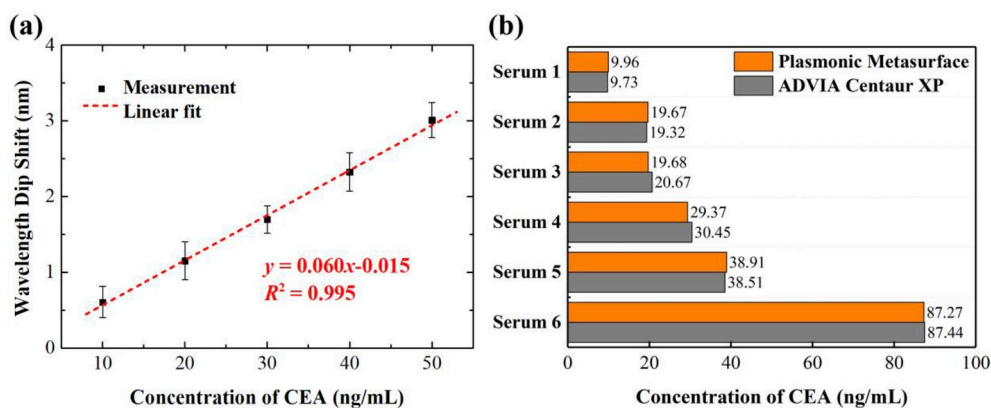
Fig. 6. (a) Plasmonic resonance wavelength shift as a function of CEA concentration. (b) Detection results of CEA from 6 serum samples using plasmonic metasurfaces in comparison with using the Siemens immunoassay system.

3.4. Tumor marker sensing and serum detection

The sensing property in Fig. 6(a) is obtained from the measurement using five different concentrations of commercial CEA solutions from 10 ng/mL to 50 ng/mL (Ameen et al., 2017). Each measurement has the same incubation time and the same solution volume in the detection chamber, and each error bar of measurement is based on *s.d.* calculation for three data points. Fig. 6(a) denotes the resonance wavelength shift as a function of the CEA concentration, which implies that the shift of spectral dip is increased proportionally to the CEA concentration. The correlation coefficient *R* of 0.995 illuminates a good linear relationship between the CEA concentration and resonance wavelength shift. The tumor marker detection of CEA in serum samples are performed by using the optimized plasmonic metasurfaces, as shown in Fig. 6(b). Compared with the results from the Siemens immunoassay system, the largest data deviation for the detected results by using the metasurfaces is less than 4.8%, which demonstrates good consistency with clinical examination in the hospital. In addition, all the detections can be done simultaneously within 30 min. The CEA concentration of about 20 ng/mL is a critical threshold for diagnosis and prognosis of cancer, so the plasmonic metasurfaces have sufficiently covered the sensing range of an effective screening for cancer, as shown in Fig. 6(b). Our experimental results indicate the promising potential of the flexible metasurfaces for practical medical applications.

4. Conclusion

In summary, the plasmonic metasurface of gold nanobump array achieved by an optimized nanofabrication process provides many advantages for tumor maker detection in human serum. The all-gold sensing surface facilitates the process of antibody functionalization that requires the metasurface to be thiolated in advance. The optimized plasmonic metasurface allows the reflection-type measurement at normal incidence, and the light source as well as the photodetector are located on the same side, which consumedly simplifies the optical detection system. The sensing spectral region are established within the operating wavelengths of silicon photodiodes, which reduces the cost of analytical instrumentation significantly. The flexible lightweight plasmonic metasurfaces based on low-cost manufacture and simple optical configuration demonstrate a promising potential for future portable medical devices/systems in point-of-care diagnosis and mobile healthcare.

Declaration of competing interest

The authors declare that they have no known competing financial interests or personal relationships that could have appeared to influence the work reported in this paper.

CRediT authorship contribution statement

Jinfeng Zhu: Conceptualization, Methodology, Resources, Software, Validation, Formal analysis, Investigation, Visualization, Supervision, Writing - original draft, Writing - review & editing, Project administration, Funding acquisition. **Zhengying Wang:** Methodology, Software, Formal analysis, Validation, Investigation, Data curation, Visualization, Writing - original draft. **Shaowei Lin:** Data curation, Validation, Investigation. **Shan Jiang:** Data curation, Validation, Investigation. **Xueying Liu:** Visualization, Writing - review & editing. **Shengshi Guo:** Validation, Investigation.

Acknowledgement

Appendix A. Supplementary data

Supplementary data to this article can be found online at https://doi.org/10.1016/j.bios.2019.111905.

References

Ameen, A., Hackett, L.P., Seo, S., Dar, F.K., Gartia, M.R., Goddard, L.L., Liu, G.L., 2017. Adv. Opt. Mater. 5 (11), 1601051.

Bouchal, P., Dvořák, P., Babocký, J., Bouchal, Z., Ligmajer, F., Hrtoň, M., Křápek, V., Faßbender, A., Linden, S., Chmelík, R., Šikola, T., 2019. Nano Lett. 19, 1242–1250.

Cai, Y., Zhu, J., Liu, Q.H., 2015. Appl. Phys. Lett. 106 (4), 043105.

Cai, J., Zhang, C., Liang, C., Min, S., Cheng, X., Li, W.-D., 2019. Adv. Opt. Mater. 1900516.

Camilo, D.E., Miyazaki, C.M., Shimizu, Flávio M., Ferreira, M., 2019. Mat. Sci. Eng. C-Mater. 102, 315–323.

Cetin, A.E., Etezadi, D., Galarreta, B.C., Busson, M.P., Eksioglu, Y., Altug, H., 2015. ACS Photonics 2 (8), 1167–1174.

Chen, Y., Zhu, J., Xie, Y., Feng, N., Liu, Q.H., 2019. Nanoscale 11, 9749–9755.

Costantini, D., Lefebvre, A., Coutrot, A.-L., Moldovan-Doyen, I., Hugonin, J.-P., Boutami, S., Marquier, F., Benisty, H., Greffet, J.J., 2015. Phys. Rev. Appl. 4 (1), 014023.

Danilova, A., Tselikova, G., Wu, F., Kravets, V.G., Ozerov, I., Bedu, F., Grigorenko, A.N., Kabashin, A.V., 2018. Biosens. Bioelectron. 104, 102–112.

Feng, L., Huo, P., Liang, Y., Xu, T., 2019. Adv. Mater. 1903787.

Ghaemi, H.F., Thio, T., Grupp, D.E., Ebbesen, T.W., Lezec, H.J., 1998. Phys. Rev. B. 58 (11), 6779–6782.

Gordon, R., Brolo, A.G., Mckinnon, A., Rajora, A., Leathem, B., Kavanagh, K.L., 2004. Phys. Rev. Lett. 92 (3), 37401.

Hwang, Y., Davis, T.J., 2016. Appl. Phys. Lett. 109, 181101.

Jackman, J.A., Ferhan, A.R., Cho, N.J., 2017. Chem. Soc. Rev. 46, 3615–3660.

Jo, N.R., Lee, K.J., Shin, Y.B., 2016. Biosens. Bioelectron. 81, 324–333.

Johnson, P.B., Christy, R.W., 1972. Phys. Rev. B. 6 (12), 4370.

Lee, J.U., Nguyen, A.H., Sim, S.J., 2015. Biosens. Bioelectron. 74, 341–346.

Liang, Y., Zhang, H., Zhu, W., Agrawal, Amit, Lezec, H., Li, L., Peng, W., Zou, Y., Lu, Y., Xu, T., 2017. ACS Sens. 2 (12), 1796–1804.

Liu, C., Meng, F., Zheng, W., Xue, T., Jin, Z., Wang, Z., Cui, X., 2016. Sens. Actuators B Chem. 228, 231–236.

Liu, B., Chen, S., Zhang, J., Yao, X., Zhong, J., Lin, H., Huang, T., Yang, Z., Zhu, J., Liu, S., Lienau, C., Wang, L., Ren, B., 2018. Adv. Mater. 30 (12), 1706031.

López-Muñoz, G.A., Estevez, M.C., Peláez-Gutierrez, E.C., Homs-Corbera, A., García-Hernandez, M.C., Imbaud, J.I., Lechuga, L.M., 2017. Biosens. Bioelectron. 96, 260–267.

Molen, K.L. Van Der, Segerink, F.B., Hulst, N.F. Van, Kuipers, L., 2004. Appl. Phys. Lett. 85 (19), 4316–4318.

Ndukaife, J.C., Mishra, A., Guler, U., Nnanna, A.G.A., Wereley, S.T., Boltasseva, A., 2014. ACS Nano 8 (9), 9035–9043.

Niu, X., Chen, H., Wang, Y., Wang, W., Sun, X., Chen, L., 2014. ACS Appl. Mater. Interfaces 6, 5152–5160.

Qin, F., Ding, L., Zhang, L., Monticone, F., Chum, C.C., Deng, J., Mei, S., Li, Y., Teng, J., Hong, M., Zhang, S., Alù, A., Qiu, C.W., 2016. Sci. Adv. 2 (1), e1501168.

Reshef, O., Saad-Bin-Alam, M., Huttunen, M.J., Carlow, G., Sullivan, B.T., Ménard, J.-M., Dolgaleva, K., Boyd, R.W., 2019. Nano Lett. 19, 6429–6434.

Singh, P., 2016. Sens. Actuators B Chem. 229, 110–130.

Špačková, B., Wrobel, P., Bocková, M., Homola, J., 2016. IEEE 104, 2380–2408.

Tang, D., Wang, C., Zhao, Z., Wang, Y., Luo, X., 2016. Laser Photonics Rev. 9 (6), 713–719.

Tokel, O., Inci, F., Demirci, U., 2014. Chem. Rev. 114 (11), 5728–5752.

Wang, D.S., Fan, S.K., 2016. Sensors 16 (8), 1175.

Wang, S., Zhan, Q., 2016. Sci. Rep. 6, 29626.

Xu, X., Peng, B., Li, D., Zhang, J., Wong, L.M., Zhang, Q., Wang, S., Xiong, Q., 2011. Nano Lett. 11 (8), 3232–3238.

Zhang, Z., Chen, Z., Wang, S., Cheng, F., Chen, L., 2015. ACS Appl. Mater. Interfaces 7, 27639–27645.

Zhang, Z., Wang, H., Chen, Z., Wang, X., Choo, J., Chen, L., 2018. Biosens. Bioelectron. 114, 52–65.

Zheng, J., Yang, W., Wang, J., Zhu, J., Qian, L., Yang, Z., 2019. Nanoscale 11, 4061–4066.

Zhou, J., Tao, F., Zhu, J., Lin, S., Wang, Z., Wang, X., Ou, J.Y., Li, Y., Liu, Q.H., 2019. Nanophotonics 8 (2), 307–316.

Zhu, J., Xue, M., Shen, H., Wu, Z., Kim, S., Ho, J.-J., Hassani-Afshar, A., Zeng, B., Wang, K.L., 2011. Appl. Phys. Lett. 98, 151110.

Zhu, J., Zhu, X., Hoekstra, R., Li, L., Xiu, F., Xue, M., Wang, K.L., 2012. Appl. Phys. Lett. 100 (14), 143109.

Zhu, J., Bai, Y., Zhang, L., Song, Z., Liu, H., Zhou, J., Lin, T., Liu, Q.H., 2016. IEEE Photonics J 8 (4), 6804107.

Zhu, J., Zhang, L., Bai, Y., Liu, H., Liu, Q.H., 2017. IEEE Photonics Technol. Lett. 29 (6), 504–506.